

# Molecular Dynamics of the tRNA<sup>Ala</sup> Acceptor Stem: Comparison between Continuum Reaction Field and Particle-Mesh Ewald Electrostatic Treatments

Mafalda Nina<sup>†</sup> and Thomas Simonson\*

Département de Biologie et Génomique Structurales, Institut de Génétique et Biologie Moléculaire et Cellulaire (C.N.R.S.), 1 rue Laurent Fries, 67404 Strasbourg-Illkirch, France

Received: October 19, 2001

Molecular dynamics simulations with an explicit solvent model are used to investigate the effect of long-range electrostatic interactions on the structure and dynamics of a 22-nucleotide RNA hairpin in solution, the *E. coli* tRNA<sup>Ala</sup> minihelix 5p-GGGGCUC(UUCG)GAGCUCC(ACCA). Two different treatments of long-range electrostatics are compared: a continuum reaction field method (CRF; two 1.2 ns simulations) and the particle-mesh Ewald method (PME; one 2.5 ns simulation). The reaction field simulations are the first for an RNA solute. The simulations converge rapidly to within 1.5 Å of each other and of the X-ray structure, despite two starting conformations (taken from the ensemble of NMR structures) that differ from each other by 3.3 Å and from the X-ray structure by 1.3 and 2.1 Å, respectively. After 1000 ps of one CRF simulation, the helix begins to unfold, with the first two base pairs opening. Except for the last part of this simulation, the RNA helical parameters and atomic fluctuations and the solvent structure around the G3•U16 wobble pair are all in good agreement with experiment and between simulations, whereas counterions are more ordered with PME than with CRF.

## 1. Introduction

Molecular dynamics (MD) simulations are being increasingly used to study the structure and motions of nucleic acids in solution. Because electrostatic interactions play an important role, they must be modeled accurately. The introduction in recent years of Ewald summation methods has led to stable trajectories over multi-nanosecond periods.<sup>1–6</sup> Because of this stability, Ewald methods are now widely viewed as the most accurate long-range electrostatic treatment for these systems.<sup>7–9</sup> In fact, for a simulation with a given electrostatic treatment to be considered accurate, the production of a stable structure that agrees with the dominant experimental conformation is necessary but not sufficient; two other conditions are needed. First, one should demonstrate that the MD structure is actually the intrinsic free energy minimum for the force field used, i.e., the free energy minimum in the limit of an infinitely large simulation box. If the experimental structure is an A helix, for example, but the intrinsic free energy minimum for the force field is a B helix, then a simulation that yields a stable A helix because of spurious periodicity effects must be viewed as incorrect. Second, not only the dominant structure but also the magnitude and time scale of the fluctuations and the relative stability of the minor conformations should be reproduced.

The first, free energy minimum condition appears to be at least partly verified for Ewald summation applied to DNA, because simulations of a 10-basepair fragment with Ewald summation and the AMBER force field<sup>10</sup> showed that the structure after 500 picoseconds of MD was independent of whether the starting conformation was an A or a B helix.<sup>11</sup> However, another study reported trapping of an RNA in a B conformation over several nanoseconds.<sup>12</sup> Detailed comparisons

have been made between Ewald summation and various cutoff schemes for DNA; see ref 13 for a detailed review. However, additional studies are needed to test the effect of Ewald summation on other molecules, including its effect on the magnitude and time scale of their fluctuations. Indeed, the Ewald method imposes a periodicity at all times that is not present even in a crystalline solid let alone a liquid. Therefore artifacts are to be expected if the simulation box size is not large enough, such as anisotropy and enhanced long-range correlations.<sup>14–17</sup> An alternative electrostatic treatment is to model distant solvent as a dielectric continuum. This method is well-established in liquid simulations and was originally used with periodic boundary conditions.<sup>18,19</sup> More recently, it has been used with finite models, such as a solute in a spherical water droplet.<sup>20–25</sup> Indeed, the equilibrium effect of solvent molecules outside the droplet can be accounted for rigorously by a potential of mean force (pmf),<sup>26,27</sup> as shown by Beglov & Roux,<sup>22</sup> and the continuum reaction field can provide an accurate approximation to the pmf.<sup>21–25</sup> This approach is being used increasingly for protein solutes<sup>28–30</sup> and is expected to be more accurate than cutoff schemes, but it has not been applied to nucleic acids so far. By comparing it to Ewald summation, the assumptions of each method can be tested for RNA solutes, and their validity for a given model size can be established.

Below, we study a 22-nucleotide RNA hairpin, 5p-GGGGCUC(UUCG)GAGCUCC(ACCA), which represents the acceptor stem fragment of the *E. coli* tRNA<sup>Ala</sup> (Figure 1). This and similar RNA “minihelices” have been shown to be substrates of their cognate aminoacyl-tRNA synthetases<sup>31,32</sup> and are thought to be early precursors of tRNA.<sup>33,34</sup> The *E. coli* tRNA<sup>Ala</sup> minihelix is one of the most extensively characterized of the tRNA minihelices. Its solution structure was determined by NMR spectroscopy;<sup>35</sup> the structure of the double helical portion was solved by X-ray crystallography.<sup>36</sup> MD simulations with Ewald boundary conditions and the AMBER force field<sup>10</sup> have also been

\* To whom correspondence should be addressed.

<sup>†</sup> Present address: Syngenta Crop Protection, WRO-1060.2.36, CH-4002 Basel, Switzerland.

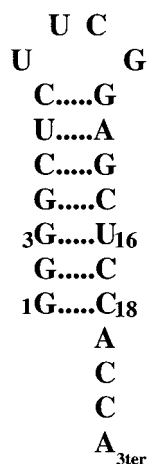


**Figure 1.** *E. coli* tRNA<sup>Ala</sup> minihelix. Secondary structure representation.

reported.<sup>37</sup> The minihelix contains a G•U wobble base pair (3•16 in Figure 1) which is the main identity element for the recognition of tRNA<sup>Ala</sup> by alanyl-tRNA synthetase (AlaRS); that is, it is largely responsible for the specificity with respect to other noncognate tRNAs or RNA minihelices.<sup>38–40</sup> The role of the wobble pair has been attributed to either direct interactions between AlaRS and the G•U pair in the RNA minor groove<sup>32</sup> or to an indirect effect, where the G•U pair promotes a local distortion of the acceptor stem that increases the AlaRS–RNA complementarity.<sup>41</sup>

To complement the earlier studies and examine the effect of different long-range electrostatic treatments, we report three MD simulations. The long-range electrostatic interactions are treated either by particle-mesh Ewald summation (PME; one simulation) with a 70 Å box length, or by the continuum reaction field method (CRF; two simulations), where the RNA and solvent within a sphere of 76 Å diameter are simulated in atomic detail, whereas the solvent outside the sphere is treated as a dielectric continuum.<sup>22</sup> In both cases, the CHARMM22 force field is employed.<sup>42</sup> The continuum reaction field simulations are the first for an RNA solute. The extent of conformational sampling and the overlap between the trajectories are characterized by a principal component analysis. For this system, solvated by approximately 8000 TIP3P water molecules,<sup>43</sup> reasonable agreement between the structures obtained from CRF and PME trajectories is found, even when they start from significantly different conformations. However, the PME simulation converges more closely toward the X-ray structure, whereas one of the CRF simulations begins to unfold after 1000 ps, suggesting that the PME electrostatic treatment may reproduce the stability of the native structure more accurately. Except for the last portion of the latter CRF trajectory, the three simulations exhibit almost identical atomic fluctuations. In contrast, the counterions are more ordered with PME than with the CRF treatment.

## 2. Methods

**Initial Structures.** The starting conformation of the minihelix was taken from the ensemble of 30 NMR structures (entry 1IKD in the Protein Data Bank).<sup>35</sup> Two simulations (S1 and S2) were started from the NMR conformation 16 (NMR-16), which has a straight helical axis, in agreement with the X-ray acceptor stem structure.<sup>36</sup> One simulation (S3) was started from NMR conformation 1 (NMR-1), which has a more bent conformation. The RNA was solvated by overlaying a large box of water and

deleting waters that overlapped the RNA. A total of 21 NH<sub>4</sub><sup>+</sup> counterions were used to neutralize the system. The counterions were initially placed at positions of low electrostatic potential. The electrostatic potential produced by the RNA was calculated at the positions of the water oxygens by solving the Poisson equation with a standard finite-difference method<sup>44</sup> (and the program UHBD<sup>45</sup>), assuming dielectric constants of 1 inside the RNA and 80 outside. The water molecule with the lowest potential was replaced by a counterion, and then the potential calculation was repeated including the first counterion, and so on, until 21 counterions were positioned. At this point, the first 10 counterions were deleted, and the procedure continued, until 21 counterions were again in place. This two-phase insertion protocol ensured that each ion was inserted on the basis of the potential of the RNA “decorated” by a cloud of at least 10 other counterions.

**Force Field Parameters.** The RNA solute was described by the 1995 version of the CHARMM22 nucleic acid force field.<sup>42</sup> Water molecules were described by a modified TIP3P model,<sup>46</sup> which has essentially the same dielectric properties<sup>47</sup> as the original TIP3P model.<sup>43</sup> Parameters for the ammonium counterions were adapted from the OPLS force field of Jorgensen et al.<sup>48</sup> and from the methylammonium parameters in the CHARMM22 force field<sup>49</sup> and tested by solvation free energy calculations, as described in the Supporting Information. The internal geometry of the water molecules, as well as all bond lengths involving hydrogens, were kept fixed with the SHAKE algorithm.<sup>50</sup>

**Molecular Dynamics Setup and Equilibration.** A first simulation (S1) used the CRF treatment of long-range electrostatic interactions.<sup>20–25</sup> The starting RNA conformation was NMR conformation 16.<sup>35</sup> A spherical region of 38 Å radius was simulated in atomic detail, including the RNA solute, 21 ammonium counterions, and 7431 water molecules, for a total of 23 111 atoms. This sphere size ensured that the minihelix had a solvation shell of explicit water at least 5 Å thick in all directions (and much thicker in most directions). The solvent outside this sphere was treated as a dielectric continuum with a dielectric constant of 80. The inner region has a dielectric of 1. Atomic partial charges in the inner region polarize the outer continuum, giving rise to a reaction field on each explicit atom, which is approximated here by a spherical harmonic expansion to order 15.<sup>20,22</sup> Within the spherical region, electrostatic interactions were treated without any truncation by using a multipole approximation for groups more than 12 Å apart.<sup>51,52</sup> van der Waals interactions were smoothly switched to zero between 8 and 10 Å. Explicit solvent molecules were also subjected to a soft, van der Waals, boundary potential to prevent them from evaporating into the outer continuum.<sup>22</sup>

The solvent molecules were first equilibrated for 100 ps with the solute and counterions fixed, using Langevin dynamics at a constant temperature of 300 K, with a friction coefficient for the water oxygen atoms corresponding to a relaxation time of 2 ps.<sup>53</sup> Next, positional restraints were applied to the minihelix heavy atoms; these were progressively released over a 180 ps period. Harmonic distance restraints were also imposed during equilibration between U8:H2' and G11:O6 and U8:O2 and G11:H1 in the UUCG loop, and between G3:O6 and U16:H3 and G3:H1 and U16:O2 in the wobble base pair and progressively released over the same period (for atom numbering in the wobble pair, see Figure 5 below). Production was carried out for 1.2 nanoseconds, using Langevin dynamics with no restraints, except for a weak harmonic restraint that maintained the RNA center of mass close to the sphere's center.

A second simulation (S2) used periodic boundary conditions and particle mesh Ewald summation to treat long-range electrostatic interactions.<sup>54,55</sup> The starting RNA conformation was the same as that for S1 (NMR-16). The simulation box consisted of a cube of 70 Å length containing the RNA, 21 counterions, and 9705 water molecules, for a total of 32 480 atoms. To calculate long-range interactions in Fourier space, atomic charges were projected onto a grid with a 1 Å spacing using cubic spline interpolation. For short-range interactions in real space, a 12 Å cutoff was used. With this setup, essentially all electrostatic interactions are explicitly evaluated. van der Waals interactions were switched to zero as for S1 above. The equilibration protocol was the same as that for S1, except that the temperature and pressure were maintained at 300 K and 1 atm by coupling to a Nose–Hoover thermostat and barostat;<sup>56,57</sup> that is, the simulation volume was allowed to fluctuate. Production was performed for 2.5 nanoseconds.

Another CRF simulation (S3) was started from NMR conformation 1 and prepared in the same way as S1. Conformation NMR-1 has some unusual, B-like features (see Table 3 below). In this simulation, the radius of the spherical dielectric and van der Waals boundaries were defined by the (fluctuating) position of the outermost water molecule. This boundary definition leads to a rigorous connection to the exact potential of mean force, as shown by Beglov & Roux,<sup>22</sup> and closely approximates a constant pressure ensemble (unlike S1, which was performed with a constant volume). The total production period was 1 ns, during which time the radius of the dielectric sphere remained very similar to the constant radius used in S1. All three simulations were done with the CHARMM program.<sup>51</sup> Including equilibration, a total of 5.4 nanoseconds of dynamics were performed.

**Principal Component Analysis.** Principal components (PCs) are collective coordinates defined so that the first  $n$  PCs represent the overall motions of the system projected into an  $n$ -dimensional space, in such a way that the projected motions reproduce the complete motions optimally in a least-squares sense.<sup>58–60</sup> Thus, the first two or three PCs provide a projection of the system’s motions into a subspace of dimension two or three, in such a way that “as much” of the true motions as possible are preserved. The PCs are eigenvectors of the atomic correlation matrix  $\sigma$ , defined by

$$\sigma_{i\alpha,j\beta} = \lambda_i \lambda_j \langle (r_{i\alpha} - \overline{r_{i\alpha}})(r_{j\beta} - \overline{r_{j\beta}}) \rangle \quad (1)$$

where  $r_{i\alpha} - \overline{r_{i\alpha}}$  is the instantaneous displacement of atom  $i$  from its mean position along the Cartesian axis  $\alpha$  ( $= x, y, \text{ or } z$ ),  $\lambda_i$  and  $\lambda_j$  are atomic weighting factors, and the brackets indicate an average over the trajectory. The weighting factors  $\lambda_i$  can be chosen to emphasize particular parts of the system or particular properties of the atoms. Below, we use the weights  $\lambda_i = \sqrt{m_i}$  for the RNA atoms and  $\lambda_i = 0$  for the solvent and counterions. With this definition, the PCs are identical to the “quasiharmonic modes of vibration”,<sup>61</sup> in which the hydrogens are given a small weight. If the motions of the system have a harmonic character, the eigenvalues  $\alpha_k$  can be converted into effective frequencies  $\omega_k$  by

$$\alpha_k = kT\omega_k^2 \quad (2)$$

where  $T$  is temperature and  $k$  is Boltzmann’s constant. For proteins and RNA molecules, the slowest motions are strongly anharmonic, whereas the fastest are nearly harmonic.

**Comparison with Nuclear Overhauser Data.** A comparison between the interproton distances derived from the NOEs and

**TABLE 1: RMS Deviation between the Experimental and MD Simulation Structures (Å)**

	S1 <sup>e</sup> (CRF)	S2 (PME)	S3 (CRF)	X-ray	NMR-16
S2 (PME)	0.7				
S3 (CRF)	1.3	1.2			
X-ray <sup>a</sup>	1.6	1.7(1.2 <sup>f</sup> )	1.1		
NMR-16 <sup>bd</sup>	2.4	2.5	2.4	2.1	
NMR-1 <sup>cd</sup>	2.1	2.0	1.9	1.3	3.3
NMR-16 stem <sup>b</sup>	1.5	2.1	2.0		
NMR-1 stem <sup>c</sup>	2.1	1.9	1.4		

<sup>a</sup> Crystal structure of the 7-bp acceptor stem of *E. coli* tRNA<sup>Ala</sup>.<sup>36</sup> (Only the first six bp were used in the analysis, because the X-ray structure has A•U instead of C•G as its seventh pair). <sup>b</sup> Initial NMR structure (PDB entry 1IKD, model 16<sup>35</sup>) for simulations S1 and S2. <sup>c</sup> Initial NMR structure (PDB entry 1IKD, model 1<sup>35</sup>) for simulation S3. <sup>d</sup> All heavy atoms except the single stranded ACCA. <sup>e</sup> Structure averaged over the first 900 ps only (see text). <sup>f</sup> Second half of the 2.5 ns trajectory.

from the S1 and S2 simulations was performed to identify possible NOE violations in the MD structures. The NOEs used in the NMR refinement correspond to 277 intraresidue-, 226 sequential-, and 62 “long-range” distances (G. Varani, personal communication). The MD average distance between two protons  $i$  and  $j$  is defined as  $\langle r_{ij}^{-6} \rangle^{-1/6}$ , where  $r_{ij}$  is the instantaneous distance and the brackets denote a time average over the MD simulation. An NOE restraint was considered violated if the average MD distance  $\pm$  its standard error was outside the restraint bounds used in the refinement. The standard error  $\sigma_{ij}$  for the mean distance  $\langle r_{ij} \rangle$  was estimated as the difference between the averages calculated from the first and second halves of the simulation.

### 3. Results

Simulations were performed with two electrostatic treatments (CRF and PME) and two starting structures that differ by 3.3 Å on average (NMR-16 and NMR-1; Table 1). In what follows, we first analyze the RNA structures from the three simulations, comparing them to each other and to the experiment. Next, we describe the fluctuations and the extent of conformational sampling in the different simulations with the help of a principal component analysis. Finally, we consider the solvent and counterion behavior and their dependency on the electrostatic treatment.

**RNA Structure. rms Coordinate Deviations.** Figure 2A shows the rms coordinate deviations of the minihelix from its mean structure during each simulation. The single-stranded ACCA region is disordered (see below) and is therefore excluded from the analysis. The deviation between each starting structure and the corresponding mean structure is shown as a short horizontal line in Figure 2A and listed in Table 1. The two starting structures, NMR-16 (S1, S2) and NMR-1 (S3), are rather different, with a mutual rms deviation of 3.3 Å. In all three simulations, the structures initially shift away from their starting conformations by 2.1–2.5 Å and move much closer to each other. Thus, during the production period, the deviation between the S2 and S3 average structures is only 1.2 Å; that between S1 and S2 is only 0.7 Å. In S2 and S3, the rms deviation from the mean fluctuates around 1.2 Å, indicating a stable mean structure. In S1, the fluctuations around the mean structure are also small until  $t = 900$  ps, when the rms increases sharply. The first two base pairs open at  $t \sim 1000$  and 1100 ps, respectively; this would probably lead to a complete unfolding of the helix if the simulation were continued.

Figure 2B shows the rms deviations from the X-ray structure (which only includes the double-stranded region). The starting

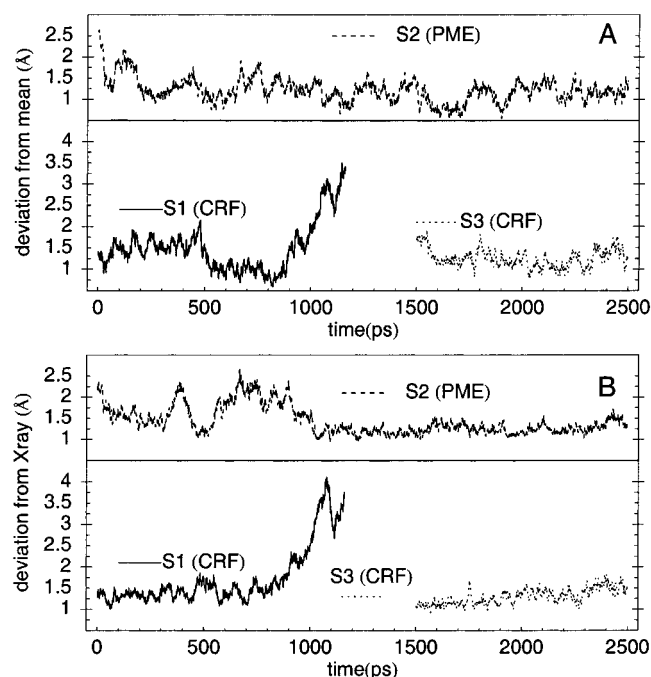


**Figure 2.** (A) RMS deviations (Å) of the instantaneous configurations along simulations S1, S2, and S3 from their respective mean structures (not including the ACCA single-stranded region or the hydrogen atoms). The short horizontal lines indicate the deviation of the starting conformation from the mean structure in each case. (B) RMS deviations (Å) of the instantaneous configurations from the X-ray structure (double-helical region only). The short horizontal lines indicate the deviation of the starting conformation from the X-ray structure in each case.

conformations NMR-16 (S1 and S2) and NMR-1 (S3) are 2.1 and 1.3 Å from the X-ray structure, respectively. During the first nanosecond of simulation, S2 shifts much closer to the X-ray structure ( $\sim 1.2$  Å deviation) and remains there for the remaining 1.5 ns. S3 starts out 1.3 Å from the X-ray structure and drifts away very slightly during production (final deviation of  $\sim 1.5$  Å). The hydrogen bond lengths for the first base pair of the stem, G1·C18, were calculated for S3 (not shown) and found to be very stable, displaying no tendency for this base pair to open. S1 shifts toward the X-ray structure during equilibration and remains close to it (deviation of  $< 1.5$  Å) until  $t = 900$  ps, when the helix begins to unfold. Thus, the three simulation structures all shift markedly toward each other and toward the X-ray structure, but S1 moves away after 900 ps.

The simulations were also compared (Figure 3, Table 1) to the NMR solution structures. Because the 30 structures in the NMR ensemble vary widely, Figure 3A gives the rms deviation between the instantaneous MD structure and the closest NMR structure during the course of S1 and S2; results for S3 are very similar. The rms deviation is between 1.25 and 2 Å most of the time, indicating good agreement, but not as good as with the X-ray structure. The instability of S1 is visible as a sharp increase near  $t = 1000$  ps. In general, we see that the movement away from the initial conformation NMR-16 is actually a conversion to other structures in the NMR ensemble. Of the 30 NMR structures, only 15 are approached during any simulation, with the three simulations approaching exactly the same NMR structures (Figure 3B). During the second half of the longer simulation S2, only three NMR conformations are visited extensively: NMR-1, NMR-17, and NMR-27. Overall, although the MD structures are compatible with the NMR data, the subset of NMR structures visited during the simulations has a much smaller spread than the complete NMR ensemble (Figure 4).

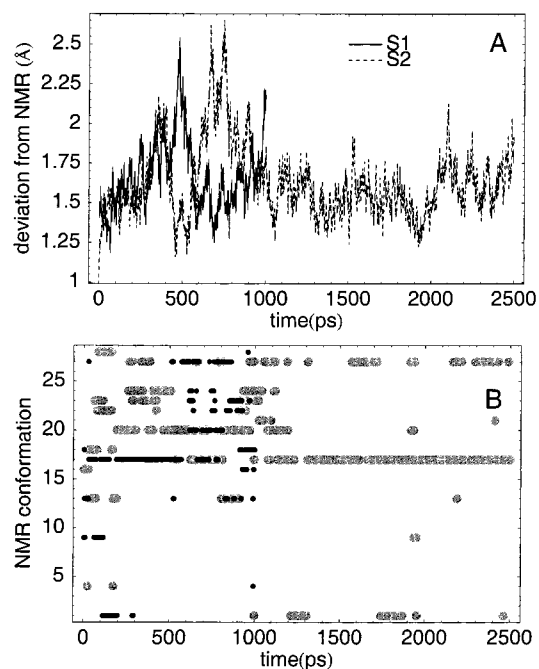


**Figure 3.** (A) RMS deviation (Å) between the instantaneous minihelix configurations along simulations S1, S2, and S3 and the closest structure from the NMR ensemble of 30 structures. Hydrogen atoms and the ACCA single-stranded region are excluded from the comparison. (B) The number of the closest NMR structure for each instantaneous conformation vs time. Black lines, S1; thick gray lines, S2. A single NMR structure is marked at each time, for each trajectory; because of the width of the marks, there appears to be overlap between different times.

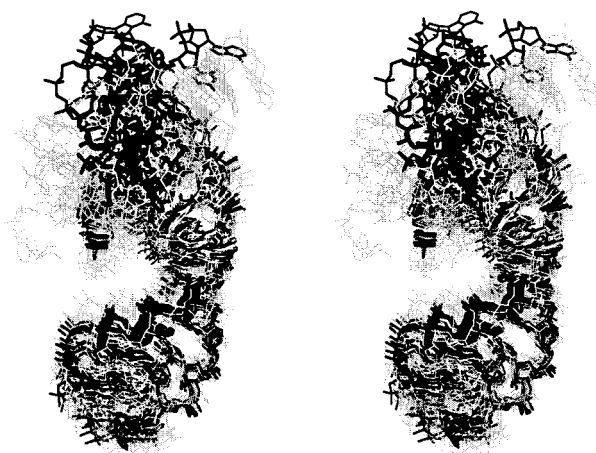


**Figure 4.** A total of 30 NMR-derived conformations. Divergent stereoview. Conformations sampled in the present MD simulations are shown in black; the others are gray (see text).

This could indicate either a lack of precision in the NMR ensemble because of the intrinsic difficulty of this structure determination technique for RNA molecules or insufficient sampling in the simulations.

To verify that the MD structures are compatible with the experimental NOE data, we compared the interproton distances derived from the NOEs and from the S1 and S2 simulations. Results are summarized in Table 2. Only NOEs with upper distance bounds of 5 Å or less were considered. Within this subset, there are seven distance violations in S1 and five in S2. These include several very slight violations in the UUCG loop (within 0.4 Å, or two standard errors of the upper NMR distance bound; see the Methods section). There are no violations in the double helical region. The only significant violations are in the

**TABLE 2: Violations of NMR Distant Restraints in Simulations S1 and S2<sup>a</sup>**

atom pairs	NMR upper bound (Å)	simulations		NMR structures
		S1 (CRF)	S2 (PME)	
Base Pairs In Stem				
G3:H8...G2:H1'	5		5.62(0.62)	4.27(0.42)
UUCG Loop				
U9:H1'...U9:H2''	3	3.08(0.06)	3.09(0.06)	2.69(0.58)
C10:H6...C10:H3'	4	4.36(0.20)	4.39(0.24)	4.03(0.05)
G11:H3'...G11:H4'	3	3.07(0.06)	3.06(0.06)	2.71(0.57)
Single Stranded ACCA				
A19:H8...C18:H1'	5	<b>6.29(0.95)</b>	5.21(0.57)	4.51 (0.61)
C20:H5...A19:H2''	5	5.23(0.99)	6.16(1.54)	4.77(1.07)
C21:H5...C20:H2''	5	<b>8.23(1.32)</b>	<b>9.49(1.54)</b>	4.13(1.14)
C21:H6...C20:H2''	4	<b>7.30(0.99)</b>	<b>8.08(1.09)</b>	3.50(1.08)
C21:H6...C20:H3'	5	5.75(1.13)	<b>6.66(0.98)</b>	3.38(0.80)
C20:H6...C20:H3'	4	<b>4.55(0.24)</b>		3.14(0.67)
A22:H8...C21:H6	5	5.56(1.25)		4.06(0.65)
C20:H5...A19:H2''	5		6.16(1.54)	4.77(1.07)
C20:H6...A19:H2''	4		5.49(1.28)	3.64(1.06)

<sup>a</sup> Significant distance violations in the MD structures are highlighted in bold. There are four in S1 and three in S2, all in the single-stranded region. The simulation values are averaged over the corresponding trajectory (standard error in parentheses). The NMR values are averaged over the 30 conformations in the NMR ensemble (standard deviation in parentheses).<sup>35</sup>

**TABLE 3: Comparison of the Average Simulated and Experimental Helix Parameters<sup>a</sup>**

	experimental structures			simulations		
	NMR-1 <sup>b</sup>	NMR-16 <sup>c</sup>	X-ray <sup>d</sup>	S1 (CRF)	S2 (PME)	S3 (CRF)
Base Pair Axis Parameters						
X disp (Å)	-4.2	-1.4	-4.3	-4.3	-4.8	-4.3
Y disp (Å)	1.1	-1.3	0.2	0.3	-0.3	-0.3
inclination (°)	26	-12	10	3	9	9
tip (°)	-5	11	-2	0	4	3
Base-Base Parameters						
shear (Å)	-0.3	-0.4	0.4	-0.5	-0.4	-0.4
stretch (Å)	0.3	-0.4	0.1	-0.2	-0.1	-0.1
stagger (Å)	-0.7	-0.6	-0.1	-0.3	-0.3	-0.2
buckle (°)	-3	-4	2	0	0	3
propeller twist (°)	-9	1	-10	-4	-7	-9
opening (°)	2	1	2	-1	0	-2
Inter Base Pair Parameters						
shift (Å)	0.3	-0.1	0.0	0.1	0.0	0.1
slide (Å)	-0.1	-0.3	-0.1	-0.3	-0.3	-0.2
rise (Å)	2.5	3.9	2.8	2.9	2.7	2.7
tilt (°)	-4	6	-1	-1	1	1
roll (°)	-2	8	1	6	3	2
twist (°)	34	29	33	29	30	31

<sup>a</sup> All calculations were performed with CURVES.<sup>62</sup> Only the double-stranded 7-bp acceptor stem of the minihelix was included in the analysis. <sup>b</sup> Initial NMR structure (conformation 1 from PDB entry 1IKD). <sup>c</sup> Initial NMR structure (conformation 16 from PDB entry 1IKD). <sup>d</sup> Crystal structure of the 7-bp acceptor stem of *E. coli* tRNA<sup>Ala</sup>.

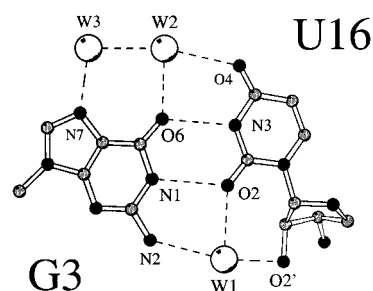
single stranded ACCA region: four in S1 and three in S2. These are due to an incorrect stacking of consecutive bases during part of the simulations. Overall, the MD structures satisfy the NOE data as well as the NMR structures, except for the single stranded ACCA region.

**Average Helical Parameters.** To characterize the shape of the helix, Table 3 reports average helicoidal parameters, including the helix axis inclination and tip and the twist between successive base pairs.<sup>62</sup> The simulations generally give mean values close to the X-ray structure. Although the overall MD helices are close to canonical A-form RNA, they are slightly underwound compared to the X-ray double-stranded region, with

**TABLE 4: Average Geometry of the G3•U16 Wobble Base Pair<sup>a</sup>**

	S1 (CRF)	S2 (PME)	X-ray <sup>b</sup>	NMR-16 <sup>c</sup>
Interatomic Distances (Å)				
U16:O2...G3:N1	3.2(0.6)	2.9(0.2)	3.0	2.7
U16:N3...G3:O6	3.3(0.9)	2.9(0.2)	2.9	3.0
U16:O2...G3:N2	4.3(0.8)	3.9(0.3)	3.9	3.2
U16:O2'...G3:O6	6.7(0.5)	6.8(0.4)	7.2	6.9
Helical Rise (Å)				
G2-C17/G3-U16	3.5(1.2)	3.5(1.0)	2.5	4.5
G3-U16/G4-C15	3.2(0.5)	3.2(0.5)	2.9	3.7
Helical Twist (°)				
G2-C17/G3-U16	10(9)	10(7)	27	18
G3-U16/G4-C15	39(4)	37(4)	39	34

<sup>a</sup> Standard deviations in parentheses. For the atom numbering, see Figure 5. <sup>b</sup> Crystal structure of the 7-bp acceptor stem of *E. coli* tRNA<sup>Ala</sup>.<sup>36</sup> <sup>c</sup> Initial NMR structure (1IKD PDB entry, model 16).<sup>35</sup>

**Figure 5.** G3•U16 wobble pair and three ordered waters observed in the crystal structure<sup>36</sup> and the simulations.

average twists of 29–31°, compared to 33° for the X-ray structure. The average overall helical axis is rather straight in the MD structures, in contrast to some very bent structures in the NMR ensemble. On average, the base-pairs are flat and nearly ideal, even though some instantaneous configurations deviate considerably (not shown). The base pair displacement away from the helix axis (“X disp” and “Y disp” in Table 3) is intermediate between the value in the NMR-16 conformation and the X-ray value and leads to a deep and narrow major groove and a shallow minor groove.<sup>63</sup> Other parameters, such as the mean base pair stretch, stagger, and opening, are in good agreement with both the NMR and X-ray structures. The sugar puckers in the minihelix were also maintained correctly throughout the simulations (not shown), except for the single stranded ACCA region where 1–2 concerted transitions occurred between the C3' endo form (predominant in the NMR ensemble) and the C2' endo form. U9 and C10 in the tetraloop were always in the correct C2' endo form.

**The G•U Wobble Pair.** The G3•U16 wobble pair corresponds to the G3•U70 pair in the complete tRNA<sup>Ala</sup> and represents the major identity element for specific tRNA<sup>Ala</sup> recognition by alanyl-tRNA synthetase.<sup>38–40</sup> Table 4 summarizes the local geometry around the G3•U16 wobble base pair from experiment and the simulations; the analysis was only done for S1 and S2. Atom numbering in the wobble pair is indicated in Figure 5. The local geometry near this pair deviates from the canonical A-form RNA, as observed by NMR chemical shift changes.<sup>64</sup> In the crystal structure, the G•U wobble pair displays a high local shear value of -2.3 Å<sup>36</sup> and has its G3-N2 amino group pointing toward the minor groove. This arrangement is very well reproduced in both S1 and S2, with local shear values of -2.8 and -2.6 Å, respectively. The experimental local “stretch” values for the wobble pair (-0.4 Å for the mean NMR structure and -0.5 Å for the X-ray structure) are higher than for other base pairs; this tendency is also well reproduced, with a value

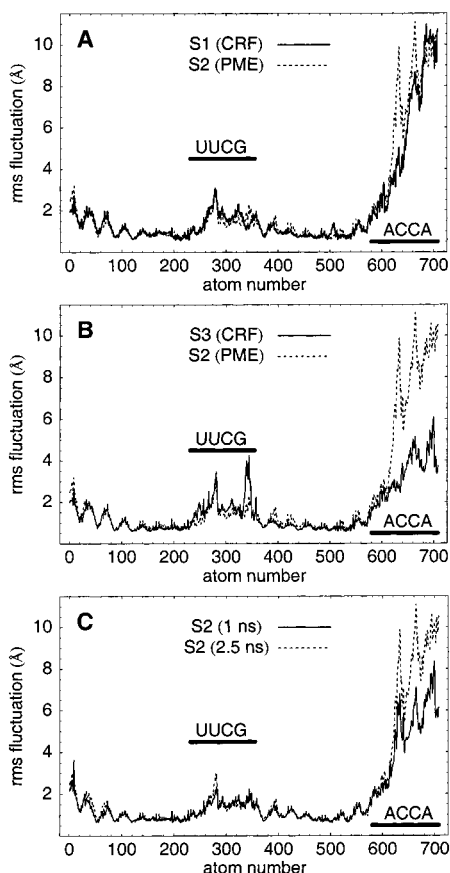


**Figure 6.** Atomic rms fluctuations ( $\text{\AA}$ ) around the mean structure for all atoms of the minihelix as a function of atom number. The UUCG loop and the single-stranded ACCA terminus are marked. Comparison between simulations. (A) S1 vs S2; (B) S2 vs S3; (C) the first nanosecond of S2, compared to the entire simulation.

of  $-0.6 \text{ \AA}$  in both simulations. The local helical twist above the G3·U16 pair is  $18^\circ$  and  $27^\circ$  for the NMR-16 initial structure and the X-ray structure, respectively. A previous simulation with the AMBER force field<sup>37</sup> gave  $17 \pm 4^\circ$ . The present simulations give somewhat smaller twist angles, with large rms fluctuations:  $10 \pm 9^\circ$  and  $10 \pm 7^\circ$  for S1 and S2, respectively. For the twist below the G3·U16 base pair, the simulations predict an angle of  $39^\circ$  (simulation S1) or  $37^\circ$  (simulation S2), in good agreement with the experimental values and the earlier simulation.<sup>37</sup> Thus, a helical underwinding is predicted above the wobble pair and an overwinding below it, as expected, but the underwinding is more pronounced than in the experimental structures or the previous simulation.

**Fluctuations and Conformational Sampling. Atomic Fluctuations.** Figure 6 shows the rms atomic fluctuations of the RNA around its mean structure for each simulation. For S1, only the first 900 ps of production are considered, because the structure begins to unfold after this period. Pairwise comparisons between the simulations are shown, and results for the first nanosecond of S2 are compared to the entire trajectory. Agreement between the simulations is excellent, except for G11 in the tetraloop, which is more mobile in S3. The largest motions are in the ACCA single-stranded region (atoms 580–708), which is highly disordered, whereas the UUCG loop (atoms 231–355) fluctuates less and the double-helical stem still less. The fluctuations from the first nanosecond of S2 are also in very good agreement with the full simulation (except for the ACCA terminus), indicating reasonable convergence with respect to simulation length. The magnitude of loop motion in simulation S2 is consistent with

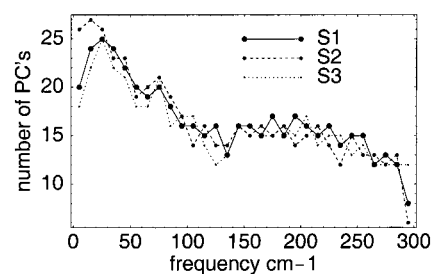


**Figure 7.** Frequency histograms giving the number of principal components (or quasiharmonic modes of vibration) of the tRNA<sup>Ala</sup> minihelix per  $10 \text{ cm}^{-1}$  frequency interval, calculated from the three simulations. (Although the frequency units are a convenient way to rank the principal components, it should be kept in mind that the corresponding motions are strongly anharmonic; see the text.)

an earlier simulation,<sup>65</sup> also performed with periodic boundary conditions and Ewald summation.

**Principal Component Analysis.** Principal component analysis is a powerful tool to characterize the low-frequency collective motions of biopolymers.<sup>58–66</sup> The PCs define conformational spaces of low-dimensionality that optimally describe the minihelix motion in a mass-weighted, least-squares sense. They are ranked by their “frequencies”, which are related to their associated eigenvalues through eq 2. It should be kept in mind that these “frequencies” do not always correspond to the actual time-scale for motion along the principal components, especially for the slowest PCs, which are very anharmonic.<sup>60,66</sup> For a study of RNA dynamics in the harmonic approximation, see ref 67.

The 500 PCs of largest amplitude, or lowest “frequency” were calculated by diagonalizing the (mass-weighted) atomic correlation matrix of the RNA (see the Methods section). The spectral density of states is shown in Figure 7. The densities from the three simulations are in very good agreement, with a broad peak around  $15\text{--}25 \text{ cm}^{-1}$  and a minimum around  $130 \text{ cm}^{-1}$ . The dot products between the PCs from the three simulations were calculated. The two slowest PCs from S1 and S2 are approximately interchanged. Thus, PC-1(S1) has a dot product of 0.77 with PC-2(S2) and a dot product of 0.32 with PC-1(S2) (perfect overlap corresponds to a dot product of unity). For PC-2(S1), the corresponding dot products are 0.76 and 0.28. The two slowest PCs from S3 are mixtures of PC-1(S2) and PC-2(S2): PC-1(S3)·PC-1(S2) = 0.61 and PC-1(S3)·PC-2(S2) = 0.55. For subsequent PCs, there is a substantial “mixing”; that is, each PC from S1 or S3 has a significant overlap with 5–6 of the S2 PCs that lie in the same amplitude range and vice versa.

As with other biopolymers,<sup>58–60</sup> the contribution of the first few PCs to the rms fluctuations is dominant, e.g. the first 30 PCs (out of 2124) account for 82–83% of the total rms atomic fluctuations. The slowest PCs correspond mainly to bending motions of the RNA. These motions are apparent in Figure 8, which shows a series of snapshots from S1.

Projecting the instantaneous displacement onto each principal component gives the principal coordinates; the first eight are plotted vs time in Figure 9 for S1 and S2. Results for S3 are similar. The first few PCs exhibit the structural transitions identified above from the analysis of the coordinate deviations (Figure 2). In S1, the movement away from the X-ray structure around  $t = 900 \text{ ps}$  is evident in PCs 1 and 3 (dashed vertical lines in Figure 9). Because these PCs decrease again after  $t = 1000 \text{ ps}$ , other more local degrees of freedom must also be involved in the unfolding. The shift of S2 toward the X-ray structure is evident in PC-1(S2). In most cases, the sampling of PCs 1–4 is incomplete, because they either have not fully

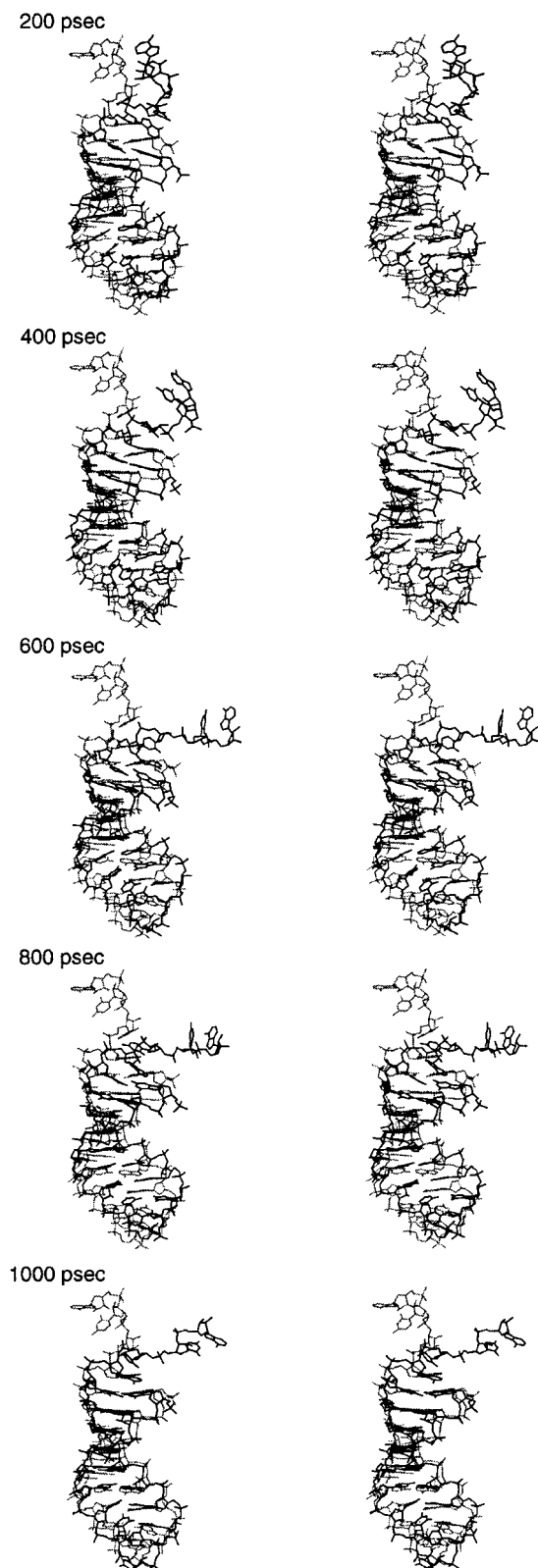


**Figure 8.** Stereoviews of five instantaneous configurations from the S1 simulation (black), compared to the NMR starting structure 16 (grey). The structures have all been oriented according to the best fit of the double-stranded region (all heavy atoms). Each snapshot is labeled by the corresponding time (200–1000 ps).

converged or describe at most one oscillation during the simulation. The other 2120 PCs from all simulations undergo at least a few oscillations during the nanosecond trajectories and are adequately sampled.

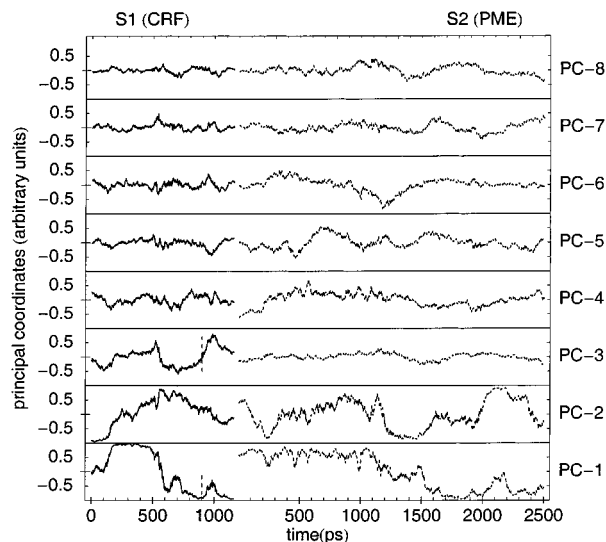


**Figure 9.** Instantaneous amplitudes (arbitrary units) vs time for the first eight principal components (the eight PCs with the largest amplitudes, or the lowest “frequencies”), calculated from S1 (solid lines) and S2 (dotted lines). Dashed vertical lines highlight a large deviation in the S1 simulation at  $t = 900$  ps (see PC-1 and PC-3 panels).

**Solvent and Counterion Structure. Hydration of the G3•U16 Wobble Pair.** The hydration of the G3•U16 wobble pair is of special interest, because ordered water molecules around this pair have been proposed to play a role in the specific recognition of the tRNA<sup>Ala</sup> minihelix by alanyl-tRNA synthetase.<sup>36,37</sup> In the minihelix X-ray structure, one ordered water molecule connects U16(O2′) to G3(N2) in the minor groove, whereas two others bridge U16(O4) and G3(N7) in the major groove (Figure 5). It was proposed that these three water molecules are integral parts of the tRNA<sup>Ala</sup> acceptor stem structure.<sup>36</sup> However, the X-ray structure was determined at 100 K, where the solvent structure could differ from that at physiological temperature. The simulations provide a detailed picture of room-temperature solvation, allowing this hypothesis to be tested.

The average water structure around the RNA is characterized here by the radial distribution functions  $g_i(r)$ , which measure the probability of finding the oxygen atom of a solvent molecule at the distance  $r$  from a particular atom  $i$  of the minihelix. The position and shape of the first peak in  $g_i(r)$  characterize the first solvation shell around the selected atoms. The integrated value of  $g_i(r)$  corresponds to the time-averaged, running coordination number of atom  $i$ .

In what follows, results from S1 (CRF electrostatics) and S2 (PME electrostatics) are compared to the X-ray structure. In the asymmetric unit of the X-ray structure, a total of 155 ordered waters were observed.<sup>36</sup> From these waters and their images by the crystal symmetry operators, the experimental, low temperature, radial distribution functions can be calculated. By construction, disordered waters in the crystal are not included; however, it is expected that these will mostly lie outside the first 1–2 solvation shells of the RNA, so they should not affect the radial distribution functions at short distances. The coordination numbers from the X-ray structure take the form of step functions here, because the crystal waters are considered completely ordered. If the (small) thermal vibrations of the crystal waters were taken into account, the step functions would be convoluted with Gaussians, leading to smoother curves. In contrast, the simulation waters fluctuate, giving smoothly varying coordination numbers and rdf's. The X-ray structure has two RNA molecules per asymmetric unit: results for each are shown separately. Differences between the two give

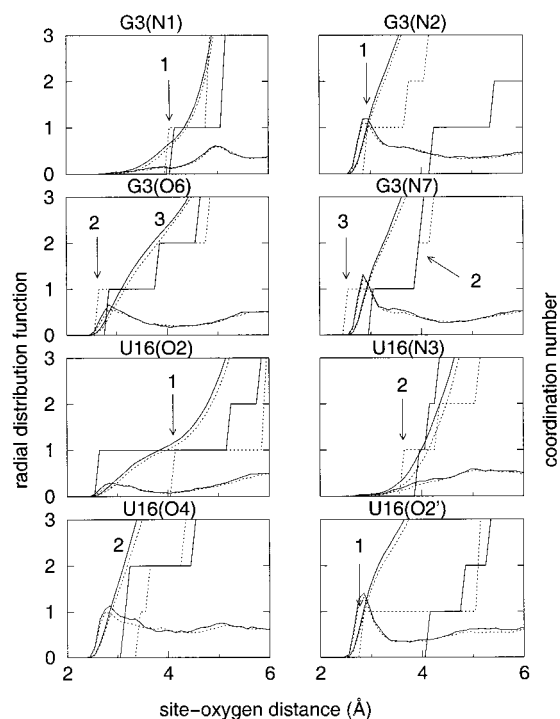


**Figure 10.** Solute-solvent radial distribution functions and running coordination numbers from simulations S1 (solid line) and S2 (dotted line). The running coordination numbers from the X-ray structure are also shown as solid and dotted lines (corresponding to the two molecules in the crystallographic asymmetric unit); they are distinguishable from the MD data because they increase in discrete steps. The distributions correspond to water around specific RNA atoms of the wobble G3·U16 pair, indicated above each panel. For the atom numbering, see Figure 5. Arrows indicate the steps associated with the three ordered waters shown in Figure 5, proposed to play a role in specific protein recognition.<sup>36</sup>

information about the stability of the different water sites, e.g., if a site is very stable, it should be occupied in both molecules.

Radial distribution functions (rdf's) and coordination numbers are displayed in Figure 10 for selected atoms of the G3·U16 wobble pair. The atom numbering is given in Figure 5. The solvation structure is remarkably similar for the CRF and PME simulations and in good agreement with the X-ray results, despite the temperature difference (room temperature vs 100 K). The steps corresponding to the three ordered X-ray waters around the G3·U16 pair are labeled in Figure 10. The MD rdf's have corresponding peaks (see G3(N2), G3(O6), and G3(N7) rdf's, respectively). In the minor groove, the MD rdf's have peaks 2.85 Å from U16(O2') and 2.95 Å from G3(N2). This is in very good agreement with the water solvating one of the RNA molecules in the X-ray structure, where the distances of water 1 to G3(N2) and U16(O2') are 2.94 and 2.95 Å, respectively.<sup>36</sup> Interestingly, the other RNA molecule in the X-ray asymmetric unit does not have a water in this position (Figure 10, G3(N2) and U16(O2') panels). The sites in the major groove (e.g., U16(O2) and U16(O4)) have much broader peaks (except for G3(N7)), indicating that water in the major groove is less structured than in the minor groove. Comparing the MD and X-ray running coordinate numbers, we see that the position of X-ray water 2 is occupied by a single MD water, but this water is rather mobile (see rdf's for U16(O4) and G3(O6)). The position of X-ray water 3 is also occupied by an MD water (see G3(N7) and G3(O6) rdf's).

For the sites other than waters 1–3, agreement between the two simulations and electrostatic treatments remains excellent,

whereas agreement with the X-ray results is more qualitative. The MD data suggest that, at room temperature, some of the sites that were ordered and fully occupied in the crystal at 100 K are not as highly ordered (U16(N3)) or are only partially occupied (U16(O2)) at room temperature.

**Counterion Structure and Mobility.** The simulations also provide a detailed description of the counterion structure and dynamics. Only a few salient features are presented here, on the basis of S1 (CRF electrostatics) and the first nanosecond of S2 (PME). Radial distribution functions (not shown) between the phosphorus atoms and the nitrogen of the NH<sub>4</sub><sup>+</sup> indicate that when an ordered ammonium site occurs, the position of the first peak (near 3.35 Å) does not depend on the electrostatic treatment. However, the occupancies of ordered ion sites differ significantly between S1 and S2. In S1 (performed with CRF), 8 of the 21 ammonium ions shifted away from their starting positions within 100 ps. Only one of these eventually settled into a stable position (previously abandoned by another of the 8); the 7 others were disordered for the rest of the simulation. A total of 11 of the 21 ions remained in their initial positions for 200–800 ps, after which they drifted away. Only one of these shifted into another stable site (abandoned in the meantime by another ion). Overall, 11 of the 21 initial sites were stable, for periods of up to 800 ps, and only two of the 21 ions moved back into a stable site after leaving their initial site.

In S2, the number of stable sites was similar (10 out of 21), but the occupancies were generally higher: three ions remained in their initial sites throughout the nanosecond of simulation, and three others were stable for 700–800 ps. In most cases, the stable ions make a single hydrogen bond to a neighboring phosphate; only one ion in each simulation bridges two phosphates. Note that there are two ordered ion sites in the crystal structure,<sup>36</sup> occupied by a sodium and a strontium ion, respectively, but neither site contacts a phosphate group.

#### 4. Conclusions

Several previous studies considered the effect of different electrostatic treatments on simulations of nucleic acids and proteins; for a detailed review, see ref 13. Most of these studies compared variants of Ewald summation to various cutoff treatments. Ewald summation and some of the cutoff methods were found to give structures that were stable and close to the experimental structures.<sup>7</sup> The accuracy of the computed fluctuations and the stability of minor conformations were more difficult to assess. None of the previous studies considered the continuum reaction field approach used here.

The most important result of this work is that all three simulations, performed with two electrostatic treatments and two significantly different structures, converge rapidly toward each other, with rms deviations of just 0.7–1.3 Å between the three average structures. Except for the last part of S1 (CRF), the simulations also converge toward the X-ray structure (S1 and S2) or remain close to it (S3), with average deviations of 1.2–1.5 Å, compared to 2.1 (S1 and S2) and 1.3 Å at the beginning. This convergence and the overall stability of the structure are especially marked in the PME simulation, S2. Apparently, the 70 Å box size is large enough to avoid artificial trapping of the RNA in its starting conformation, and the force field has a genuine preference for the X-ray, rather than the starting, NMR-16 conformation.

A second result is that one of the two CRF simulations begins to unfold after 1000 ps of production. This could be a random event, which would only occur very rarely in a large series of

simulations. The experimental characteristic time for base opening at a helix terminus is not known.<sup>68</sup> Alternatively, it could be the sign of a systematic instability with CRF electrostatics (for this model size). Note that CRF simulations of another RNA helix were stable over a similar timescale (unpublished data). If there is a systematic instability with CRF, it could presumably be eliminated by using a somewhat larger simulation model, i.e., more explicit water and/or counterions. Indeed, the PME simulation above included 30% more water than the CRF simulations (9705 vs 7431 molecules). The unfolding may be facilitated by the faster dynamics that are known to occur with models including continuum solvent (because of the lack of dielectric and mechanical friction), compared to models with only explicit solvent.<sup>69,70</sup>

Despite the differences in long-time behavior between the simulations, the short-range RNA structure is in very good agreement between simulations and in reasonable agreement with experiment (Tables 3 and 4). All three simulations have mean structures that satisfy the experimental NOE restraints (Table 2). The CHARMM22 force field is seen to perform very well. One exception is the exaggerated underwinding above the wobble pair (Table 4), which is not observed with the AMBER force field.<sup>37</sup> Other such cases of force-field dependence of nucleic acid structure have been reported in the past.<sup>71,72</sup> The water structure near the G3·U16 wobble pair is almost identical in the S1 and S2 simulations (Figure 10), despite the different electrostatic treatments. This lends support to previous analyses of hydration patterns around RNA base pairs in MD simulations, which have mainly been based on simulations using Ewald summation; see refs 7 and 73 and references therein. Three ordered waters found in the low temperature (100 K) crystal structure were also observed here. In contrast, the counterion behavior depends on the electrostatic treatment. Although the number of ordered counterion sites is almost the same with CRF and PME, the site occupancies are higher with PME.

Neither of the electrostatic methods used here is exact (contrary to occasional statements in the literature<sup>8</sup>). However, both have a sound physical basis and are well-established in liquid simulations, so that good agreement is expected as long as the models sizes are large enough and sufficient sampling is performed. The mean structures from the three simulations are indeed in good agreement with each other and with the experiment, if the S1 unfolding event is excluded. The motions along the faster degrees of freedom are also very similar, suggesting that these degrees of freedom are adequately modeled and adequately sampled. The possibility of a systematic instability with CRF and this model size remains open; repeated (and expensive) simulations with a larger CRF model are needed to analyze this possibility in detail.

**Acknowledgment.** M.N. acknowledges a Long Term Fellowship awarded by the European Molecular Biology Organization. We thank G. Varani for providing us with the set of experimental NMR restraints; M. Karplus for the CHARMM program; and B. Hartmann, B. Roux, D. Beglov, R. Lavery, and M. Karplus for helpful discussions. Some of the simulations were done at the CINES Supercomputer Center of the Ministry of Education (supercomputer allocation c20010722229 to T.S.).

**Supporting Information Available:** Parameters for the ammonium counterions adapted from the OPLS force field of Jorgensen et al.<sup>48</sup> and from the methylammonium parameters in the CHARMM22 force field<sup>49</sup> and tested by solvation free energy calculations. This material is available free of charge via the Internet at <http://pubs.acs.org>.

## References and Notes

- Zichi, D. *J. Am. Chem. Soc.* **1995**, *117*, 2957–2969.
- York, D.; Yang, W.; Lee, H.; Darden, T.; Pedersen, L. *J. Am. Chem. Soc.* **1995**, *117*, 5001–5002.
- Cheatham, T.; Miller, J.; Fox, T.; Darden, T.; Kollman, P. *J. Am. Chem. Soc.* **1995**, *117*, 4193–4194.
- Yang, L.; Pettitt, B. *J. Phys. Chem.* **1996**, *100*, 2564–2566.
- Young, M.; Ravishanker, G.; Beveridge, D. *Biophys. J.* **1997**, *73*, 2313–2336.
- Auffinger, P.; Westhof, E. *J. Mol. Biol.* **1997**, *269*, 326–341.
- Auffinger, P.; Westhof, E. *Curr. Opin. Struct. Biol.* **1998**, *8*, 227–236.
- Sagui, C.; Darden, T. *Annu. Rev. Biophys. Biomol. Struct.* **1999**, *28*, 155–179.
- Beveridge, D.; McConnell, K. *Curr. Opin. Struct. Biol.* **2000**, *10*, 182–196.
- Cornell, W.; Cieplak, P.; Bayly, C.; Gould, I.; Merz, K.; Ferguson, D.; Spellmeyer, D.; Fox, T.; Caldwell, J.; Kollman, P. *J. Am. Chem. Soc.* **1995**, *117*, 5179–5197.
- Cheatham, T.; Kollman, P. *J. Mol. Biol.* **1996**, *259*, 434–444.
- Cheatham, T.; Miller, J.; Spector, T.; Cieplak, P.; Kollman, P. In *Molecular modelling of nucleic acids*; American Chemical Society: Washington, D. C., 1997; pp 285–302.
- Norberg, J.; Nilsson, L. *Biophys. J.* **2000**, *79*, 1537–1553.
- Smith, P.; Pettitt, B. *J. Chem. Phys.* **1996**, *105*, 4289–4293.
- Boresch, S.; Steinhauser, O. *Ber. Bunsen-Ges. Phys. Chem.* **1997**, *101*, 1019–1029.
- Hunenberger, P.; McCammon, J. *Biophys. Chem.* **1999**, *78*, 69–88.
- Weber, X.; Hunenberger, P.; McCammon, J. *J. Phys. Chem. B* **2000**, *104*, 3668–3675.
- Barker, J.; Watts, R. *Mol. Phys.* **1973**, *26*, 789–792.
- Allen, M.; Tildesley, D. *Computer Simulations of Liquids*; Clarendon Press: Oxford, U.K., 1991.
- Kirkwood, J. *J. Chem. Phys.* **1934**, *2*, 351–361.
- Alper, H.; Levy, R. *J. Chem. Phys.* **1993**, *99*, 9847–9852.
- Beglov, D.; Roux, B. *J. Chem. Phys.* **1994**, *100*, 9050–9063.
- Wang, L.; Hermans, J. *J. Phys. Chem.* **1995**, *99*, 12001–12007.
- Essex, J.; Jorgensen, W. *J. Comput. Chem.* **1995**, *16*, 951–972.
- Nina, M.; Beglov, D.; Roux, B. *J. Phys. Chem. B* **1997**, *101*, 5239–5248.
- Kirkwood, J. *J. Chem. Phys.* **1935**, *3*, 300–313.
- Roux, B.; Simonson, T. *Biophys. Chem.* **1999**, *78*, 1–20.
- Marchand, S.; Roux, B. *Proteins* **1998**, *33*, 265–284.
- Kitao, A.; Hayward, S.; Go, N. *Proteins* **1998**, *33*, 496–517.
- Simonson, T. *J. Phys. Chem. B* **2000**, *104*, 6509–6513.
- Francklyn, C.; Schimmel, P. *Nature* **1989**, *337*, 478–481.
- Musier-Forsyth, K.; Scaringe, S.; Usman, N.; Schimmel, P. *Proc. Natl. Acad. Sci. U.S.A.* **1991**, *88*, 209–213.
- Rodin, S.; Rodin, A.; Ohno, S. *Proc. Natl. Acad. Sci. U.S.A.* **1996**, *93*, 4537–4542.
- Chihade, J.; Schimmel, P. *Proc. Natl. Acad. Sci. U.S.A.* **1999**, *96*, 12316–12321.
- Ramos, A.; Varani, G. *Nucl. Acids Res.* **1997**, *25*, 2083–2090.
- Mueller, U.; Schübel, H.; Sprinzl, M.; Heinemann, U. *RNA* **1999**, *5*, 670–677.
- Nagan, M.; Kerimo, S.; Musier-Forsyth, K.; Cramer, C. *J. Am. Chem. Soc.* **1999**, *121*, 7310–7317.
- Hou, Y.; Schimmel, P. *Nature* **1988**, *333*, 140–145.
- McClain, W.; Foss, K. *Science* **1988**, *240*, 793–796.
- Musier-Forsyth, K.; Schimmel, P. *Acc. Chem. Res.* **1999**, *32*, 368–375.
- Gabriel, K.; Schneider, J.; McClain, W. *Science* **1996**, *271*, 195–197.
- Mackerell, A.; Wiorkiewicz-Kuczera, J.; Karplus, M. *J. Am. Chem. Soc.* **1995**, *117*, 11946–11975.
- Jorgensen, W.; Chandrasekar, J.; Madura, J.; Impey, R.; Klein, M. *J. Chem. Phys.* **1983**, *79*, 926–935.
- Warwicker, J.; Watson, H. *J. Mol. Biol.* **1982**, *157*, 671–679.
- Madura, J.; Briggs, J.; Wade, R.; Davis, M.; Luty, B.; Ilin, A.; Antosiewicz, J.; Gilson, M.; Baheri, B.; Scott, L.; McCammon, J. *Comput. Phys. Comm.* **1995**, *91*, 57–95.
- Neria, E.; Fischer, S.; Karplus, M. *J. Chem. Phys.* **1996**, *105*, 1902–1921.
- Höchtel, P.; Boresch, S.; Bitomsky, W.; Steinhauser, O. *J. Chem. Phys.* **1998**, *109*, 4927–4937.
- Jorgensen, W.; Gao, J. *J. Phys. Chem.* **1986**, *90*, 2174–2182.
- Mackerell, A.; Bashford, D.; Bellott, M.; Dunbrack, R.; Evanseck, J.; Field, M.; Fischer, S.; Gao, J.; Guo, H.; Ha, S.; Joseph, D.; Kuchnir, L.; Kuczera, K.; Lau, F.; Mattos, C.; Michnick, S.; Ngo, T.; Nguyen, D.; Prodhom, B.; Reiher, W.; Roux, B.; Smith, J.; Stote, R.; Straub, J.;

Watanabe, M.; Wiorcikiewicz-Kuczera, J.; Yin, D.; Karplus, M. *J. Phys. Chem. B* **1998**, *102*, 3586–3616.

(50) Ryckaert, J.; Ciccotti, G.; Berendsen, H. *J. Comput. Phys.* **1977**, *23*, 327–341.

(51) Brooks, B.; Brucoleri, R.; Olafson, B.; States, D.; Swaminathan, S.; Karplus, M. *J. Comput. Chem.* **1983**, *4*, 187–217.

(52) Stote, R.; States, D.; Karplus, M. *J. Chim. Phys.* **1991**, *88*, 2419–2433.

(53) Brünger, A. T.; Brooks, C. L.; Karplus, M. *Chem. Phys. Lett.* **1984**, *105*, 495–500.

(54) Darden, T.; York, D.; Pedersen, L. *J. Chem. Phys.* **1993**, *98*, 10089–10092.

(55) Essmann, U.; Perera, M.; Berkowitz, T.; Darden, T.; Lee, H.; Pedersen, L. *J. Chem. Phys.* **1995**, *103*, 8577–8593.

(56) Nose, S. *J. Chem. Phys.* **1984**, *81*, 511–519.

(57) Hoover, W. *Phys. Rev. A* **1985**, *31*, 1695–1697.

(58) Amadei, A.; Linssen, A.; Berendsen, H. *Proteins* **1993**, *17*, 412–425.

(59) Hayward, S.; Kitao, A.; Hirata, F.; Go, N. *J. Mol. Biol.* **1993**, *234*, 1207–1217.

(60) Garcia, A.; Soumpasis, D.; Jovin, T. *Biophys. J.* **1994**, *66*, 1742–1755.

(61) Karplus, M.; Kushick, J. *Macromolecules* **1981**, *14*, 325–332.

(62) Lavery, R.; Sklenar, H. *J. Biomol. Struct. Dynam.* **1989**, *6*, 655–667.

(63) Saenger, W., Ed.; *Principles of nucleic acid structure*; Springer-Verlag: New York, 1984.

(64) Limmer, S.; Reif, B.; Ott, G.; Arnold, L.; Sprinzl, M. *FEBS Lett.* **1996**, *385*, 15–20.

(65) Miller, J.; Kollman, P. *J. Mol. Biol.* **1997**, *270*, 436–450.

(66) Simonson, T.; Perahia, D. *Far. Discuss.* **1996**, *103*, 71–90.

(67) Matsumoto, A.; Tomimoto, M.; Go, N. *Eur. Biophys. J.* **1999**, *28*, 369–379.

(68) Guéron, M.; Leroy, J. *Methods Enzymol.* **1995**, *261*, 383–413.

(69) Potter, M.; Kirchhoff, P.; Carlson, H.; McCammon, J. *J. Comput. Chem.* **1999**, *20*, 956–970.

(70) Tsui, V.; Case, D. *J. Am. Chem. Soc.* **2000**, *122*, 2489–2498.

(71) Feig, M.; Pettitt, B. *J. Phys. Chem. B* **1997**, *101*, 7361–7363.

(72) Mackerell, A. *Molecular modelling of nucleic acids*; American Chemical Society: Washington, DC, 1997; pp 285–302.

(73) Feig, M.; Pettitt, B. *Structure* **1998**, *6*, 1351–1354.